ISSN 1674-1056
http://cpb.iphy.ac.cn
http://iopscience.iop.org/cpb
中国物理 B
Chinese Physics
中国物理 Chinese Physics B

Crystal structures and sign reversal Hall resistivities in iron-based superconductors $Li_x(C_3H_{10}N_2)_{0.32}FeSe$ (0.15 < *x* < 0.4)

Rui-Jin Sun(孙瑞锦), Shi-Feng Jin(金士锋), Jun Deng(邓俊), Mu-Nan Hao(郝木难), Lin-Lin Zhao(赵琳琳), Xiao Fan(范晓), Xiao-Ning Sun(孙晓宁), Jian-Gang Guo(郭建刚), Lin Gu(谷林)

Citation: Chin. Phys. B . 2019, 28(6): 067401. **doi:** 10.1088/1674-1056/28/6/067401
Journal homepage: http://cpb.iphy.ac.cn; http://iopscience.iop.org/cpb

What follows is a list of articles you may be interested in

Low-energy (40 keV) proton irradiation of $YBa_2Cu_3O_{7-x}$ thin films:Micro-Raman characterization and electrical transport properties

San-Sheng Wang(王三胜), Fang Li(李方), Han Wu(吴晗), Yu Zhang(张玉), Suleman Muḥammad(穆罕默德苏尔曼), Peng Zhao(赵鹏), Xiao-Yun Le(乐小云), Zhi-Song Xiao(肖志松), Li-Xiang Jiang(姜利祥), Xue-Dong Ou(欧学东), Xiao-Ping Ouyang(欧阳晓平)

Chin. Phys. B . 2019, 28(2): 027401. **doi:** 10.1088/1674-1056/28/2/027401

Superconductivity with peculiar upper critical fields in quasi-one-dimensional Cr-based pnictides

Guang-Han Cao(曹光旱), Zeng-Wei Zhu(朱增伟)

Chin. Phys. B . 2018, 27(10):107401. **doi:** 10.1088/1674-1056/27/10/107401

0-π transition induced by the barrier strength in spin superconductor Josephson junctions

Wen Zeng(曾文), Rui Shen(沈瑞)

Chin. Phys. B . 2018, 27(9): 097401. **doi:** 10.1088/1674-1056/27/9/097401

Nonlinear uniaxial pressure dependence of the resistivity in $Sr_{1-x}Ba_xFe_{1.97}Ni_{0.03}As_2$

Hui-Can Mao(毛慧灿), Dong-Liang Gong(龚冬良), Xiao-Yan Ma(马肖燕), Hui-Qian Luo(罗会仟), Yi-Feng Yang(杨义峰), Lei Shan(单磊), Shi-Liang Li(李世亮)

Chin. Phys. B . 2018, 27(8): 087402. **doi:** 10.1088/1674-1056/27/8/087402

Effect of Mn substitution on superconductivity in iron selenide (Li, Fe)OHFeSe single crystals

Yiyuan Mao(毛义元), Zian Li(李子安), Huaxue Zhou(周花雪), Mingwei Ma(马明伟), Ke Chai(柴可), Shunli Ni(倪顺利), Shaobo Liu(刘少博), Jinpeng Tian(田金鹏), Yulong Huang(黄裕龙), Jie Yuan(袁洁), Fang Zhou(周放), Jianqi Li(李建奇), Kui Jin(金魁), Xiaoli Dong(董晓莉), Zhongxian Zhao(赵忠贤)

Chin. Phys. B . 2018, 27(7): 077405. **doi:** 10.1088/1674-1056/27/7/077405

Crystal structures and sign reversal Hall resistivities in iron-based superconductors $Li_x(C_3H_{10}N_2)_{0.32}FeSe$ ($0.15 < x < 0.4$)*

Rui-Jin Sun(孙瑞锦)[1,2], Shi-Feng Jin(金士锋)[1,3,†], Jun Deng(邓俊)[1,2], Mu-Nan Hao(郝木难)[1,2], Lin-Lin Zhao(赵琳琳)[1,2], Xiao Fan(范晓)[1,2], Xiao-Ning Sun(孙晓宁)[1,2], Jian-Gang Guo(郭建刚)[1,2], and Lin Gu(谷林)[1,2,‡]

[1] *Beijing National Laboratory for Condensed Matter Physics, Institute of Physics, Chinese Academy of Sciences, Beijing* 100190, *China*
[2] *University of Chinese Academy of Sciences, Beijing* 100049, *China*
[3] *School of Physical Sciences, University of Chinese Academy of Sciences, Beijing* 101408, *China*

(Received 8 March 2019; revised manuscript received 10 April 2019; published online 8 May 2019)

Heavy electron-doped FeSe-derived materials have attracted attention due to their uncommon electronic structures with only 'electron pockets', and they are different from other iron-based superconductors. Here, we report the crystal structures, superconductivities and normal state properties of two new Li-doped FeSe-based materials, *i.e.*, $Li_{0.15}(C_3H_{10}N_2)_{0.32}FeSe$ (P-4) and $Li_x(C_3H_{10}N_2)_{0.32}FeSe$ ($P4/nmm$, $0.25 < x < 0.4$) with superconducting transition temperatures ranging from 40 K to 46 K. The determined crystal structures reveal a coupling between Li concentration and the orientation of 1,3-diaminopropane molecules within the largely expanded FeSe layers. Superconducting fluctuations appear in the resistivity of the two superconductors and are fitted in terms of the quasi two-dimensional (2D) Lawrence–Doniach model. The existence of a crossing point and scaling behavior in the T-dependence of diamagnetic response also suggests that the two superconductors belong to the quasi-2D system. Interestingly, with the increase of temperature, a sign of Hall coefficient (R_H) reversing from negative to positive is observed at $\sim$ 185 K in both phases, suggesting that 'hole pockets' emerge in these electron-doped FeSe materials. First principle calculations indicate that the increase in FeSe layer distance will lift up a 'hole band' associated with $d_{x^2-y^2}$ character and increase the hole carriers. Our findings suggest that the increase in two dimensionalities may lead to the sign-reversal Hall resistivity in $Li_x(C_3H_{10}N_2)_{0.32}FeSe$ at high temperature.

Keywords: superconductor, Lawrence–Doniach model, dimensionality

PACS: 74.70.–b, 74.70.Xa **DOI:** 10.1088/1674-1056/28/6/067401

1. Introduction

The Fermi surface (FS) topology has been considered as a key ingredient in understanding the mechanism of the iron-based superconductors (SCs). As revealed by angle-resolved photoemission spectroscopy (ARPES) and band structure calculations, the superconductivity and normal state of Fe-based SCs are governed by their electronic structure involving the Fe 3*d* orbitals crossing the Fermi energy. In iron-pnictide materials, the electronic structure usually consists of hole pockets near the Brillouin zone center (Γ point) and electron pockets near the Brillouin zone corners (M point).[1] The electron scattering between the electron and hole pockets gives rise to a sign-reversed s-wave pairing,[2,3] as proposed by the spin-fluctuation-mediated $s\pm$ pairing theory. As for the iron-selenide superconductors, experimental evidence suggests quite a similar pairing mechanism for the bulk FeSe and Fe(Te,Se).[4,5] However, the discovery of heavily electron doped (HED) FeSe-based SCs, including $A_xFe_{2-y}Se_2$ (A = K, Rb, Cs, Tl),[6,7] monolayer FeSe thin films grown on $SrTiO_3$,[8] and the recently discovered (Li, Fe)OHFeSe (FeSe-11111),[9–11] raise a challenge to the aforementioned pairing mechanism. Based on the extensive investigation of ARPES[7,9,12] and STM,[13] it is now widely accepted that the 'hole pockets', which are crucial in the above pairing mechanism, do not exist in these superconductors.

Without electron doping, FeSe is a typical compensated semimetal with its FS consisting of both hole and electron bands.[1,12] In fact, the Hall coefficient of bulk FeSe changes sign several times with rising temperature.[14] A notable feature of this compound is that it undergoes a 'nematic' structural transition at $T_s \sim 87$ K, below which the Fermi surface is still comprised of hole bands, but the Hall resistivity becomes negative.[12] High pressure can depress the nematic phase and significantly increase the T_c of pristine FeSe from 8 K up to 37 K.[15,16] Meanwhile, Sun *et al.* recently reported that the normal-state Hall resistivity of FeSe also changed sign from negative to positive under high pressure,[17] demonstrating enlarged hole pockets and enhanced interband

*Project supported by the National Natural Science Foundation of China (Grant Nos. 51472266, 51532010, 91422303, and 51772323), the National Key Research and Development Program of China (Grant No. 2016YFA0300301), and the Key Research Program of Frontier Sciences, Chinese Academy of Sciences (Grant No. QYZDJ-SSW-SLH013).

†Corresponding author. E-mail: shifengjin@iphy.ac.cn
‡Corresponding author. E-mail: l.gu@iphy.ac.cn

© 2019 Chinese Physical Society and IOP Publishing Ltd

spin fluctuations, similar to the observations in high-T_c pnictide systems. However, the FS topology of FeSe-based materials is dramatically changed when sufficiently high electron-doping ($\sim 10^{21}$/cm^3) is introduced, leading to an uncommon FS consisting of only 'electron pockets'.[7,8,10] Unlike the scenario on FeSe, subsequent Hall resistivity measurements on $A_xFe_{2-y}Se_2$ and (Li,Fe)OHFeSe,[18–21] indicates neither the elevating temperature nor applied extremely high pressure will lead to sign reversal of Hall coefficient, indicating that in these materials the 'hole bands' are far below the Fermi energy. Meanwhile, a sign reversal of Hall resistance with temperature rising was observed in few-layered FeSe film deposited on $SiTO_3$ substrate,[22] suggesting the 'hole pockets' reemerged in electron-doped few-layered FeSe films. Considering the difference in response of Hall resistance between bulk $A_xFe_{2-y}Se_2$ or (Li,Fe)OHFeSe material and few-layered FeSe film, it may suggest that the sign change of the Hall constant can be related to the decrease of dimensionality. To answer that question, it is significant to investigate the crystal structures and temperature-dependent hall resistivities of another family of quasi-2D FeSe superconductors, *i.e.*, the FeSe intercalated by large organic molecules.

In this study, we report the crystal structures, superconductivities and Hall s of 1,3-diaminopropane molecular intercalated FeSCs, $Li_x(C_3H_{10}N_2)_{0.32}FeSe$ ($x = 0.15$, $0.2 \sim 0.4$). Our results demonstrate that the two new high-T_c superconducting phases with FeSe layer distance extended up to ~ 10.9 Å. Further fitting to the resistivity in terms of the Lawrence–Doniach model and the results of T-dependent diamagnetic responses suggest that the superconductivities in the two compounds possess obvious quasi-2D characteristics. Interestingly, a sign of Hall coefficient (R_H) reversing from negative to positive is observed at ~ 185 K in both superconducting phases with temperature increasing, whether their symmetries and doping levels are different or not. First principle calculations reveal that the increase in FeSe layer distance will lift up a 'hole band' associated with $d_{x^2-y^2}$ character, and significantly increase the hole carriers around Γ point.

2. Experimental method

All sample manipulations were carried out in an argon-filled dry box with an O_2 and H_2O content below 1 ppm. Tetragonal $Fe_{1+\delta}$ Se was synthesized following the method described in Ref. [12]. Anhydrous 1,3-diaminopropane (1,3-DIA) (Sinopharm Chemical Reagent, 99.0% purity) was purified following the method in Ref. [23]. Polycrystalline $Li_x(C_3H_{10}N_2)_yFeSe$ ($x = 0.15$, 0.2, 0.25, 0.4, 0.6) samples were prepared by the solvent-thermal method. In a typical synthesis, 0.0045-mole $Fe_{1+\delta}$ Se powder, nominal-mole-ratio Li pieces (Alfa Aesar, 99.9% purity) and 10-mL ultra-dried 1,3-diaminopropane were placed in a silica ampoule and then sealed. The ampule was heated at 473.15 K for 12 h in an oven, followed by opening the ampoule in an argon-filled dry box and thoroughly rinsing with fresh 1,3-diaminopropane. Finally, the solvent was removed under vacuum, and the dark black product was loaded into the measurement cell for characterizing the structure and physical properties.

The x-ray powder diffraction patterns were used for the characterizing the phase and structure solution. Room temperature power x-ray diffraction (PXRD) spectra of nominal $Li_x(C_3H_{10}N_2)_yFeSe$ ($x = 0.15$, 0.2, 0.25, 0.4, 0.6) were collected by using a PANalytical X'pert Pro diffractometer with Cu Kα radiation (40 kV, 40 mA) and a graphite monochromator in a reflection model ($2\theta = 5^\circ$ to 80°, step $= 0.017^\circ$ (2θ)). Well-grounded fine powder samples on glass slides were loaded into a homemade airtight accessory to prevent the sample from oxidizing during collecting the diffraction pattern. Laboratory *in situ* PXRD measurements were made by using a Rigaku SmartLab instrument (Cu Kα radiation) equipped with an Anton Paar HTK-600 N oven sample stage (10^{-2} Pa, 80 K–300 K). The room-temperature diffraction pattern (at 300 K) was first obtained as a standard, and the low temperature data were collected over the 2θ range of 5°–100° in steps of 0.017° at 85 K, 130 K, 150 K, 170 K, 200 K, 250 K, respectively. Structure determination and Rietveld refinement were performed using Fullprof suites. For solving the structures, $C_3H_{10}N_2$ molecular and FeSe layers were used as independent motifs in a simulated annealing approach, a preliminary structural model is built up with space group P-4 (phase I) and $P4/nmm$ (phase II), and then Li position is located by Fourier difference analysis. Finally, Rietveld refinement against the PXRD data was obtained based on this structure model, with the site occupancies constrained to the sample composition during the refinement.

The sample composition (Li:Fe:Se) were determined by inductively coupled plasma mass spectrometry (ICP-AES). The nitrogen content in each of the samples was determined by using an oxygen and nitrogen analyzer (ONA, Senbao TN-306, Shanghai), with a stand deviation of 0.1 ppm and nitrogen concentration in a range between 0.0005% and 20%.

Magnetization and resistivity measurements were carried out using a SQUID PPMS-9 system (quantum design). Magnetic susceptibility measurements were made in a direct current (DC) field of 40 Oe (1 Oe = 79.5775 A·m^{-1}) and a temperature range of 10 K–300 K after cooling in zero applied field and in the measuring field. To ensure metallic contact between the polycrystalline grains, the resistivity and Hall measurement were conducted based on the pressurized samples that are further annealed at 150 °C for 12 h. Temperature dependence of the resistivity $\rho(T)$ of $Li_x(C_3H_{10}N_2)_{0.32}FeSe$ was measured in a standard four-probe configuration with an applied current of less than 2 mA. The Hall coefficient (R_H) of

$Li_x(C_3H_{10}N_2)_{0.32}FeSe$ was obtained by a linear fit of ρ_{xy} and B from -9 T to 9 T at each of the temperatures of 50 K, 100 K, 150 K, 200 K, 250 K, and 300 K.

The first principles calculations were performed with the Vienna *ab-initio* simulation package (VASP).[24,25] We employ the generalized gradient approximation (GGA) in the form of the Perdew–Burke–Ernzerhof (PBE) for the exchange–correlation potential.[26] The energy cut-off for the plane wave expansion is 500 eV. The Brillouin zones were sampled by the Monkhorst–Pack method with meshes of $9 \times 9 \times 12$. The structural model of FeSe and $Li_{0.15}(C_3H_{10}N_2)_{0.32}FeSe$ were based on the experimental structure parameters. The model of $(C_3H_{10}N_2)_{0.32}FeSe$ was made by omitting the Li in $Li_{0.15}(C_3H_{10}N_2)_{0.32}FeSe$, which is appropriate to evaluating the influence of expanded layer distance on electronic structure. To simplify calculations, we omitted the charge neutral 1,3-DIA molecules. Doping was simulated by adding extra electrons into the system, together with a compensating uniform positive background. The added electrons were 0.15 "extra" electrons per Fe atom compared with stoichiometric FeSe, which was in consistent with the experimental result.

3. Results and discussion

3.1. Molecule intercalated phases

Figure 1(a) shows the PXRD patterns of the as-synthesized compounds co-intercalated by 1,3-DIA molecules and Li metal ions with nominal compositions $Li_x(C_3H_{10}N_2)_yFeSe$ ($x = 0$, 0.15, 0.2, 0.25, 0.4, and 0.6). With the assistance of highly reductive lithium solution ($0.15 < x < 0.6$), a series of new phases with much enhanced lattice parameters appear. The first phase pure sample without residue FeSe is obtained at $x = 0.15$ (phase I). Based on extinction conditions, the diffraction peaks of phase I is indexed into a primitive tetragonal cell, with lattice parameters $a = 3.8136(4)$ Å and $c = 10.617(1)$ Å. With the increase of Li concentration ($0.15 < x < 0.25$), the initial set of reflections rapidly diminishes and is replaced by a new set of reflections. The new phase (phase II) without residue phase I is first obtained at $x = 0.25$, and the pattern is indexed into a primitive tetragonal supercell, with lattice parameters $a = 3.7906(2)$ Å and $c = 21.632(1)$ Å. Strikingly, the diffraction profiles of the new tetragonal phase persist up to $x = 0.4$, suggesting that the phase II tolerates an Li concentration range c from $x = 0.25$ to 0.4. Finally, phase II is decomposed at sufficiently high Li concentration ($x > 0.4$), with a considerable quantity of impurities Li_2Se appearing at $x = 0.6$. The lattice parameters of the phases at different nominal x values are summarized in Table 1. It is worth noting that the tunable dopant concentrations in $Li_x(C_3H_{10}N_2)_yFeSe$ (phase II, $0.25 \leq x \leq 0.4$) are in contrast to the discreet metal concentrations found in known intercalated FeSe systems,[27,28] suggesting that the organic molecule intercalated FeSe may serve as an ideal platform to investigate the influence of carrier concentration on the superconductivity in FeSe system.

As shown in Table 1, the ICP-AES analyses indicate that slight lithium loss occurs during the reaction. Meanwhile, the ONA analyses indicate that the intercalated molecules are almost invariant with x value increasing, assuming that all nitrogen species come from $C_3H_{10}N_2$ molecules. The measured compositions of the two phase pure samples at $x = 0.15$, $0.25 \sim 0.4$ are $Li_{0.13}(C_3H_{10}N_2)_{0.32}FeSe$ and $Li_x(C_3H_{10}N_2)_{0.33}FeSe$ ($x = 0.22 \sim 0.34$), respectively.

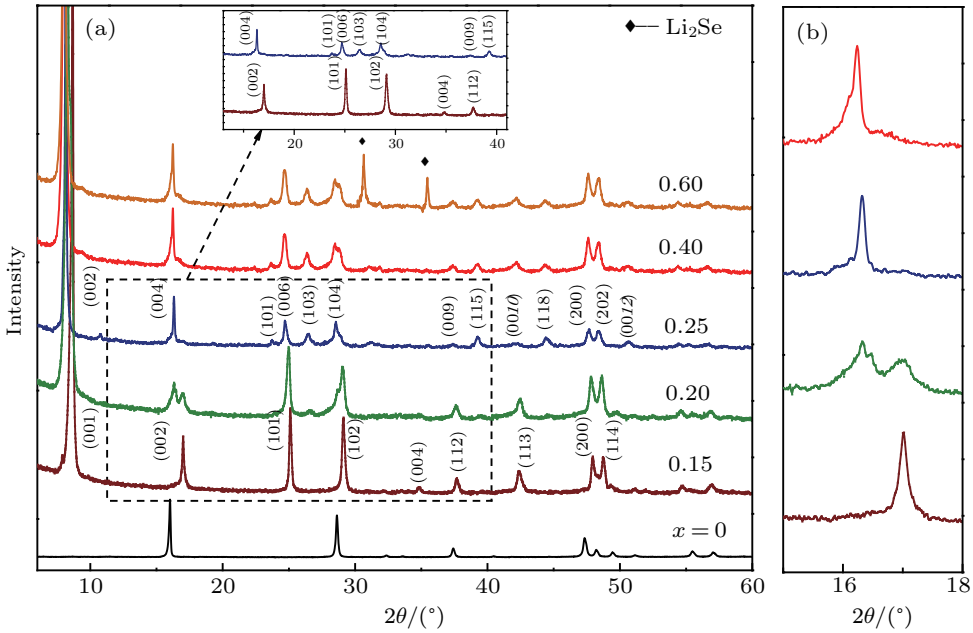


Fig. 1. (a) Powder x-ray diffraction patterns of $Li_x(C_3H_{10}N_2)_yFeSe$, with inset showing enlarge view of XRD patterns of $x = 0.15$ and 0.25, and (b) enlarged view of (00l) peak, showing a two-phase region between $x = 0.15$ and $x = 0.25$.

Table 1. Chemical analyses and crystallographic parameters from indexed PXRD data at 298 K for $Li_x(C_3H_{10}N_2)_yFeSe$.

Nominal x	ICP-AES x	y	Symmetry	a/Å	c/Å
0.15	0.13	0.32	P-4	3.8136(4)	10.617(1)
0.20	0.18	0.32	phase I+II	–	–
0.25	0.22	0.33	$P4/nmm$	3.7906(2)	21.632(1)
0.40	0.34	0.32	$P4/nmm$	3.7858(1)	21.904(5)
0.60	0.42	0.32	phase II + Li_2Se	3.7878(3)	21.912(4)

3.2. Crystal structures

As shown in Fig. 2(a), the crystal structure of $Li_{0.15}(C_3H_{10}N_2)_{0.32}FeSe$ (phase I, space group P-4) is resolved by *ab initio* structure determination from PXRD data. Rietveld refinement is performed based on this structure model and produces a satisfactory fit to the diffraction pattern, with $R_p = 2.35\%$ and $R_{wp} = 3.56\%$ at 295 K. As shown in Fig. 1(a), the intercalated $C_3H_{10}N_2$ molecules are centered at the general crystallographic positions 4h site: (x, y, z), and disordered over four diagonal orientations. Under the refined structure model, the two shortest H–Se distances in the compound are 2.765(4) Å and 2.779(2) Å, respectively, which are in consistence with those in the normal hydrogen bonding interactions.[27,29] The two Fe atoms are located at 1a site: (0, 0, 0) and 1c site: (1/2, 1/2, 0), and the Se atoms are located at 2g (0, 1/2, z) site. Li ions are located at the position adjacent to the FeSe layers at sites 2g (0, 1/2, z) site. Moreover, the compressed $FeSe_4$ tetrahedra found in $Fe_{1+\delta}$ Se are retained, with Se–Fe–Se bond angles of 104.0(1)° and 112.3(1)° compared with values of 103.9(2)° and 112.3(4)° in $Fe_{1+\delta}$ Se.[12]

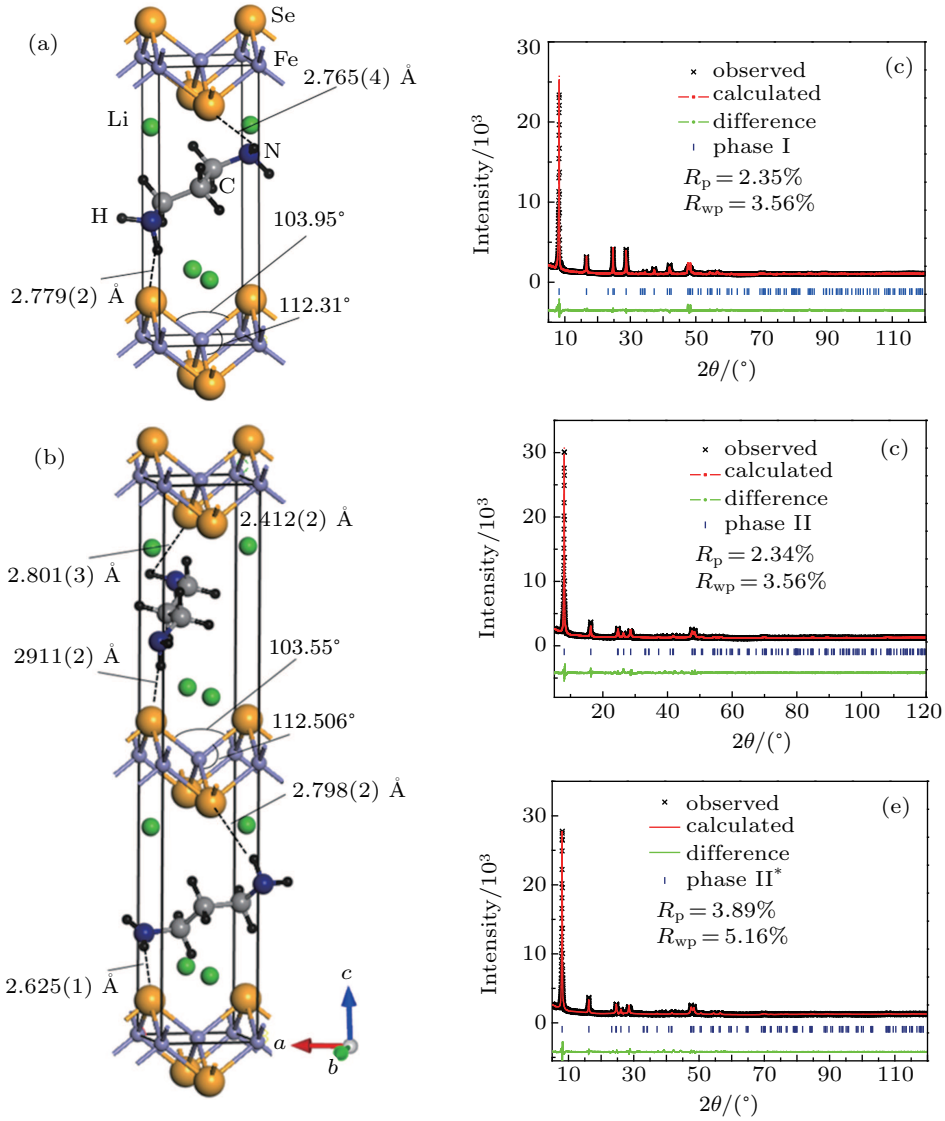


Fig. 2. Crystal structures and Rietveld refinements for two phases in 1,3-DIA intercalated FeSe at 300 K. (a) Structural model of phase I. (b) Structural model with orientational disorder of molecules for phase II ($x = 0.25$). (c) Refinement against powder x-ray diffraction data of phase I ($x = 0.15$). (d) Refinement against powder x-ray diffraction data of phase II ($x = 0.25$). (e) Refinement against powder x-ray diffraction data of phase II ($x = 0.4$).

As shown in Fig. 2(b), the crystal structure of $Li_{0.25}(C_3H_{10}N_2)_{0.33}FeSe$ (phase II) is successfully determined in a similar manner in space group $P4/nmm$. The main structural difference between the two phases lies in the fact that with Li concentration increasing, the orientations of the intercalated molecules in phase II between the adjacent FeSe layers become inequivalent to each other. Subsequently, the unit cell is doubled along the c axis. Along with the phase transition, the FeSe interlayer distance is further extended from 10.617 Å to 10.816 Å. There is also hydrogen bonding between the hydrogen atoms and the anion of FeSe layers, with the short H–Se bond distances being around 2.63 Å–2.91 Å.[27,29] Moreover, the $FeSe_4$ tetrahedra in phase II become more distorted with electron doping increasing. As shown in Fig. 1, the Se–Fe–Se bond angles increases from 112.31° to 112.51°, the values are comparable to the results in ammonia intercalated $Li_{0.6(1)}(ND_2)_{0.2(1)}(ND_3)_{0.8(1)}$ Fe_2Se_2 (112.84(3)°).[27] As shown in Fig. 1(e), we also refine the crystal structure of phase II compound at $x = 0.4$, with the final reliability factors $R_p = 3.89\%$ and $R_{wp} = 5.16\%$ reached. The refined structural parameters confirm that the doping continuously increases the distortion of $FeSe_4$ tetrahedron, with the Se–Fe–Se angle further increasing to 112.61°. Meanwhile, the anion height within the FeSe layer also monotonically increases from 1.491(6) Å ($x = 0.15$) to 1.497(3) Å ($x = 0.4$).

3.3. Low-temperature crystal structures

For iron pnictide, a tetragonal-to-orthorhombic structural transition (from $C4$ symmetry to $C2$ symmetry) is often observed in the under-doped state. To determine the evolution of $Li_x(C_2H_8N_2)_{0.5}Fe_2Se_2$ crystal structure at low temperatures, x-ray powder-diffraction data are collected for the least electron doped sample ($x = 0.15$) at $T = 85$ K, 110 K, 130 K, 150 K, 170 K, 200 K, and 295 K, respectively. Figures A2–A8 shows the observed, calculated, and difference diffraction profiles for $Li_{0.15}(C_3H_0N_2)_{0.32}Fe_2Se_2$. The low temperature patterns can all be well fitted by the room temperature structure model in the space group P-4, indicating no 'nematic' phase transition occurring between 85 K and 250 K. The temperature-dependent unit-cell parameters a and c values, the Se–Fe–Se bond angles, Fe–Se bond lengths as well as the anion height at the measured temperatures are plotted in Figs. 3(a)–3(d) respectively. From 85 K to room temperature, the lattice parameter a increases only by 0.075%, whereas the lattice parameter c expands more obviously by 0.25%. The temperature-dependent structural details are presented in Fig. 3.

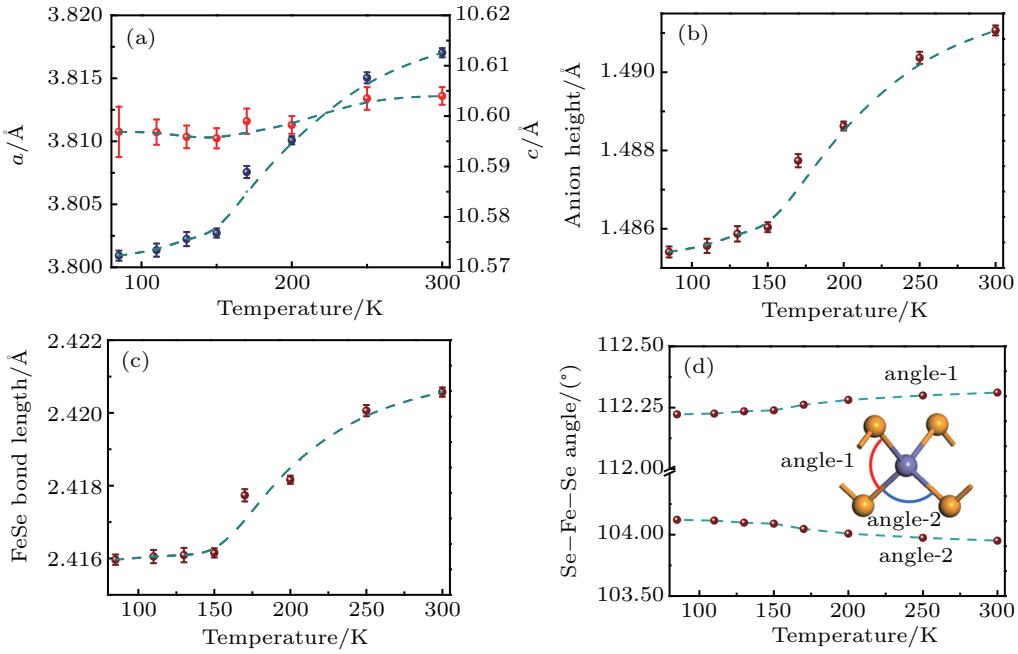


Fig. 3. Response of lattice parameters, anionic Se height, Fe–Se bond length and Se–Fe–Se bond angles of $Li_{0.15}(C_3H_{10}N_2)_{0.32}FeSe$ to elevating temperature at 85 K, 110 K, 130 K, 150 K, 170 K, 200 K, and 295 K, respectively. Dashed lines are guides for the eyes.

3.4. Quasi-2D Superconductivity behavior

Figure 4(a) shows the plots of temperature-dependent zero-field cooling (ZFC) magnetic susceptibility of three phase pure $Li_x(C_2H_8N_2)_yFe_2Se_2$ ($x = 0.15, 0.25, 0.4$) samples under an external magnetic field of 10 Oe. The magnetization of the three samples in the whole temperature range up to 300 K are presented in Figs. A9–A11. With the carrier doping from intercalated Li, sharp transitions from normal state to superconducting state are observed at temperature range from 40 K to 45 K in the measured samples. Meanwhile, no noticeable magnetization anomaly is found beyond T_c (Fig. A11), indicating no nematic phase transition occurring in the com-

pounds, which is in consistent with the powder XRD data. In Figs. 4(b) and A12–A14 we also present the resistivity data of the three compounds, respectively. Similarly, no resistivity kink that may correspond to nematic phase transition is presented in a temperature range from 20 K to 300 K.

The as-synthesized $Li_{0.15}(C_3N_2H_{10})_{0.33}Fe_2Se_2$ shows a diamagnetic transition at T_c up to 40 K with a considerable shielding fraction of 49% at 10 K in the zero-field-cooling condition. Further confirmation of superconductivity is shown in Fig. 4(b), which shows the temperature-dependent electrical resistivity measured on cold-pressed pellets. Apart from the metallic normal state above the T_c in $Li_{0.15}(C_3N_2H_{10})_{0.32}Fe_2Se_2$, a rapid decrease of resistivity appears around 40 K, and zero resistivity is reached at 37 K. With further increasing doping concentration in phase II, the maximum T_c up to 45 K is realized in $Li_{0.25}(C_3N_2H_{10})_{0.33}Fe_2Se_2$, equal to the optimal T_c value of the ammonia-intercalated FeSe. Correspondingly, the electrical resistivity shows the transition around 45 K, and zero resistivity is realized at 42 K. From $x = 0.25$ to 0.4, the T_c is found to slightly depress to 44 K at high Li concentration, indicating that the system enters into an over-doped region. Meanwhile, the superconducting volume fraction continually increases with x value increasing for two phase II samples, with their maximum value reaching 76%, confirming the bulk superconductivity.

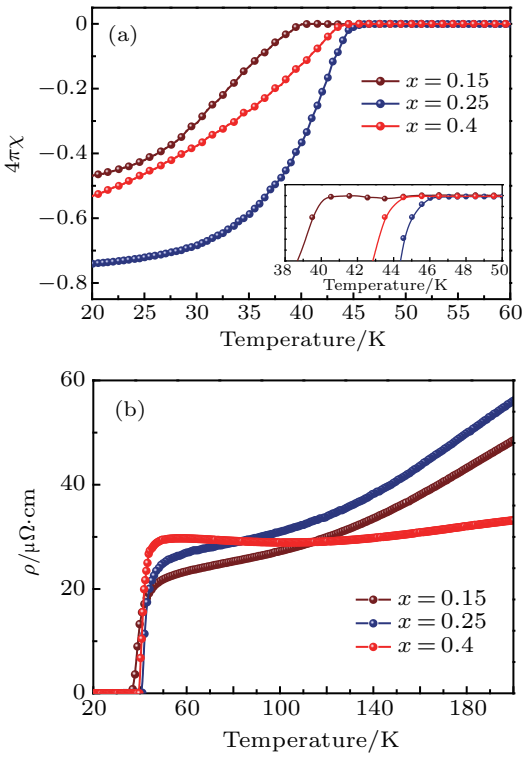


Fig. 4. (a) Magnetic susceptibilities of three phase of pure $Li_x(C_3H_{10}N_2)_yFeSe$ ($x = 0.15$, 0.25, 0.4) with inset showing enlarged view. (b) Electrical resistivity of three phase of pure $Li_x(C_3H_{10}N_2)_yFeSe$ ($x = 0.15$, 0.25, 0.4) samples.

For the $Li_x(C_3H_{10}N_2)_{0.32}FeSe$ sample, the intercalation of 1,3-DIA molecule significantly enlarges the distance between the adjacent superconducting FeSe layers, which will weaken the correlation strength along the c-axis for this FeSCs system. The effects of fluctuation on transport property and thermodynamic property are studied for classical layered superconductors, and more extensively, for the high-T_c materials. Figures 5(a) and 5(c) display the curves of temperature-dependent electric resistivity of $Li_x(C_3H_{10}N_2)_{0.32}FeSe$ at several temperatures, respectively, for the cases of $x = 0.15$ and 0.25. As a signature of the quasi-2D superconductivity in $Li_x(C_3H_{10}N_2)_{0.32}FeSe$, the resistivity transition near T_c^{onset} becomes too smooth to determine a mean-field transition point, especially in the presence of a magnetic field. Under zero magnetic field, the transition range from T_c^{onset} to T_c^{zero} of the two samples are quite narrow, *i.e.*, sample $x = 0.15$ is in a temperature range of 40 K–37 K and sample $x = 0.25$ is in a temperature from 45 K to 42 K. Such narrow transitions are comparable to the transitions of many single crystal samples as shown in Ref. [30], indicating good sample homogeneity. Under external magnetic fields from 0 T to 9 T, the diamagnetic responses of the two samples each show obviously a tailing effect, while the shift of T_c^{onset} is not obvious. This unusual behavior, which has been observed also in high-quality single crystals of layered high-T_c materials,[31] has been attributed to the effect of superconducting fluctuations in quasi-2D superconductors.

The fluctuation magnetoconductivity above the superconducting transition temperature (T_c) is hence analyzed in terms of the Lawrence–Doniach (LD) (Eqs. (1) and (2)) approach for 2D superconductivity[31,32]

$$\Delta\sigma_{LD} = \frac{e^2}{64\pi\hbar}\frac{1}{h}\int_{-\pi/s}^{\pi/s} dkz\left[\Psi^1\left(\frac{\varepsilon+h+\omega_{kz}^{LD}}{2h}\right) - \Psi^1\left(\frac{c+h+\omega_{kz}^{LD}}{2h}\right)\right], \quad (1)$$

$$\omega_{kz}^{LD} = \gamma[1-\cos(kzs)]/2. \quad (2)$$

Here, Ψ^1 is the first derivative of digamma function, e is the electron charge, h is the reduced magnetic field, ε is the $\ln(T/T_c^{mid})$, s is the distance between adjacent FeSe layers, and r is a fitting parameter corresponding to coherence length amplitude $\zeta(0)$. Figure 5(b) presents the fluctuation contribution to the conductivity $\Delta\sigma$ which varies with temperature under external magnetic fields from 0 T to 9 T. The $\Delta\sigma$ is obtained from $\rho(T)_H$ through $\Delta\sigma = 1/\rho(T)_H - 1/\rho_B(T)_H$, where the background resistivity $\rho_B(T)_H$ is obtained for each field by a linear fit from 55 K to 60 K, above the onset of fluctuation effects. The fittings lead to an averaged $\zeta(0) = 0.9652$ Å, a value which is one order of magnitude smaller than the FeSe inter-layer distance. As shown in the inset of Fig. 5(b), the experimental $\Delta\sigma$ value strongly deviates from the calculated one from the 3D anisotropic Ginsburg–Landau

(GL) model, and accords well with that from the Lawrence–Doniach model, clearly showing that the superconductivity of $Li_{0.15}(C_3H_{10}N_2)_{0.32}FeSe$ is quasi-two-dimensional in nature. Moreover, the fitting also yields a zero-temperature upper critical field $H_{c2}(0)$ = 89 T. As for $Li_{0.25}(C_3H_{10}N_2)_{0.33}FeSe$, a similar quasi-two-dimensional superconducting behavior also clearly exists. The fitting based on the Lawrence–Doniach function yields a coherence length amplitude ζ (0)=0.8425 Å, and the zero-temperature upper critical field $H_{c2}(0)$ is obtained to be 82 T.

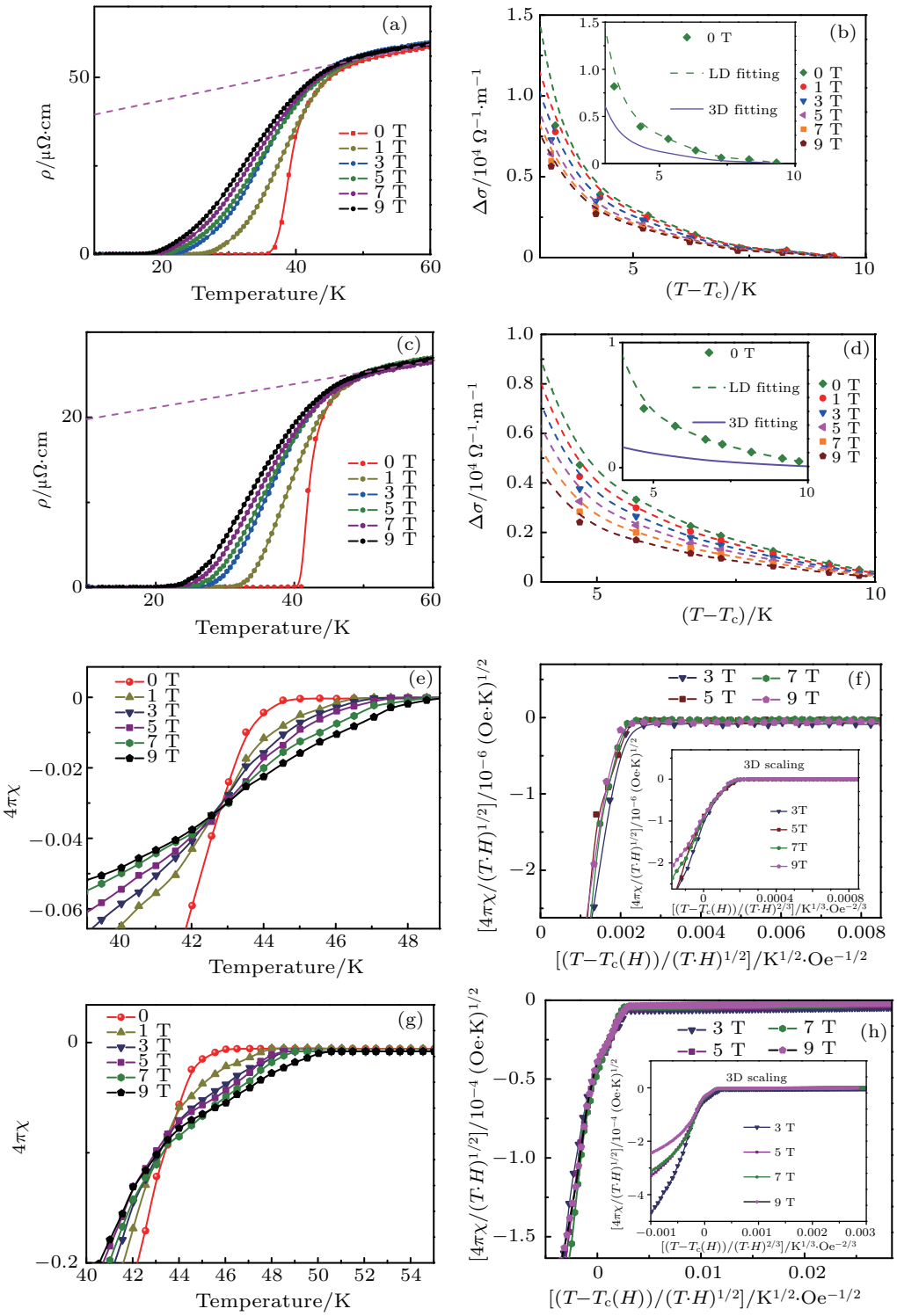


Fig. 5. Quasi-2D superconductivity behavior of $Li_x(C_3H_{10}N_2)_{0.32}FeSe$ ($x = 0.15, 0.25$). (a) and (c) Temperature-dependent resistivity around T_c of $Li_x(C_3H_{10}N_2)_{0.32}FeSe$ ($x = 0.15, 0.25$) under increasing magnetic fields. The lines are for examples (for $\mu_0 H = 9$ T) of background contribution, as determined by a linear fit above 42 K, where fluctuation effects are expected to be negligible. (b) and (d) The fluctuation contribution to the conductivity $\Delta\sigma$ varies with temperature under external magnetic fields up to 9 T for $Li_x(C_3H_{10}N_2)_{0.32}FeSe$ ($x = 0.15, 0.25$). The inset shows the fitting of $\Delta\sigma$ *versus* temperature with the quasi-2D Lawrence–Doniach model (green dash line) and 3D anisotropic Ginsburg–Landau model (brown solid line). (e) and (g) Expanded view of temperature dependence of magnetization for $Li_x(C_3H_{10}N_2)_{0.32}FeSe$ ($x = 0.15, 0.25$) under external magnetic fields. The data are corrected for T-independent background. (f) and (h) 2D scaling of high-field magnetization curves for $Li_x(C_3H_{10}N_2)_{0.32}FeSe$ ($x = 0.15, 0.25$), with inset showing 3D scaling behavior.

Figures 5(e) and 5(g) show the magnetization curves on an expanded scale close to the superconducting transition for $Li_x(C_3H_{10}N_2)_{0.32}FeSe$ ($x = 0.15,\ 0.25$) under external fields $H = 1$ T to 9 T. The data are corrected for the T-independent diamagnetic normal-state magnetization. A peculiarity of both sets of data is the existence of a crossing point $M(T,H)$ at which the magnetization is field independent. This unusual behavior is also attributed to the effect of superconducting fluctuations in quasi-two-dimensional superconductors, a similar effect has been observed in $Bi_2Sr_2CaCu_2O_8$.[33] Besides the crossing point, the scaling behavior in the diamagnetic response is also widely used to judge the dimensionality of materials.[34,35] For the temperature-dependent diamagnetization a scaling form is expected to be a function of the following form $4\pi\chi/(T\cdot H)^n = F[[T - T_c(H)]/(T\cdot H)^n]$ under the external magnetic field H, where F is a scaling function, $n = 2/3$ for anisotropic 3D material, and $n = 1/2$ for a 2D system.[34] Figures 5(f) and 5(h) show the magnetization data under fields from 0 T to 9 T that are scaled in the proper two-dimensional form and three-dimensional form (inset), respectively. For both of the compounds, the two-dimensional scaling has apparently higher quality than the three-dimensional scaling, the observations further confirm that the superconducting fluctuation is large due to the strong two dimensionality of $Li_x(C_3H_{10}N_2)_{0.32}FeSe$ ($x = 0.15, 0.25$).

3.5. Hall resistivity

In Fig. 6, we show the transport properties of $Li_x(C_3H_0N_2)_yFe_2Se_2$ ($x = 0.15,\ 0.25,\ 0.4$) samples at a normal state. In the whole temperature region, Hall resistivity $\rho_{xy}(\mu_0 H)$ of $Li_{0.15}(C_3H_{10}N_2)_{0.32}FeSe$ sample shows good linear relation against magnetic field up to 9 T. The derived Hall coefficient $R_H = \rho_{xy}/\mu_0 H$ at 9 T exhibits strong temperature dependence (Fig. 6(a)). The R_H is negative below 200 K and the absolute values decrease rapidly with temperature increasing. Finally, the R_H becomes positive at higher temperature, *i.e.*, there is a sign change at $\sim$ 185 K. It suggests that there exist two different types of charge carriers in $Li_{0.15}(C_3H_{10}N_2)_{0.32}FeSe$, the dominant carriers are of electron-type at low temperatures and become hole-type carriers at high temperature.

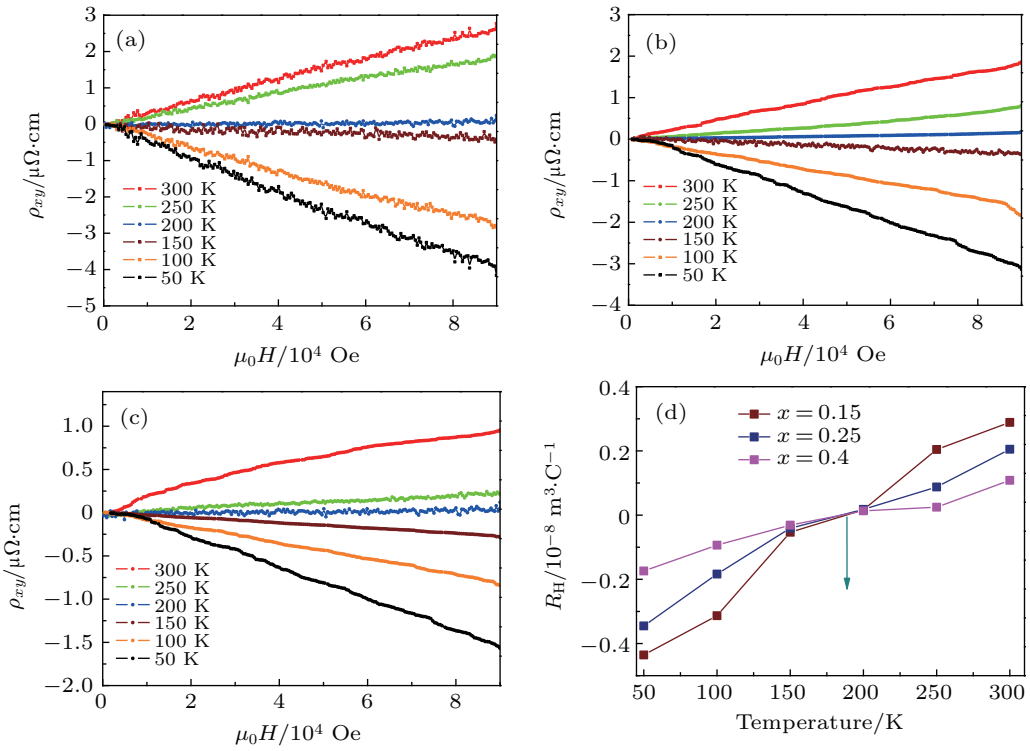


Fig. 6. Hall effect transverse resistivity ρ_{xy} measurement. (a)–(c) Field-dependent Hall effect transverse resistivity ρ_{xy} for $Li_x(C_3H_0N_2)_yFe_2Se_2$ ($x = 0.15,\ 0.25,\ 0.4$) samples. (d) Temperature-dependent Hall coefficient for three samples, R_H changes sign from negative to positive at a similar point about 185 K, demonstrating dominant hole carriers appear above 185 K.

For electron-doped FeSe materials, including KFe_2Se_2,[7] K-coated FeSe,[8] and (Li, Fe)OHFeSe,[10] the intensive ARPES and STM results both confirm that there exist only electron pockets in their electronic structures.[36] A reasonable scenario based on these results is that the low temperature Fermi surface topology in $Li_x(C_3H_{10}N_2)_yFeSe$ should also include only electron pocket, and no hole carriers should be present in the compounds. Therefore, the observed sign change of Hall resistivity R_H at $\sim$ 185 K should be a direct evidence that the 'hole pocks' originally lacking in other

'electron-doped FeSe materials reoccur in the Fermi surfaces of $Li_x(C_3H_{10}N_2)_yFeSe$ at high temperatures.

Figures 6(b) and 6(c) show the plots of Hall resistivity ρ_{xy} *versus* $\mu_0 H$ respectively for two phase II samples with much higher dopant concentration $x = 0.25$ and 0.4,. The increase of Li concentration significantly reduces the absolute value of $\rho_{xy}(\mu_0 H)$ of each sample above T_c. Strickingly, as shown in Fig. 6(d) and Table 2, the R_H values of both samples also increase rapidly with temperature rising, and their signs change at almost the same temperature (around 185 K). The values of Hall resistivity $\rho_{xy}(\mu_0 H)$ of samples $x = 0.12$ and 0.25 show similar linear dependence on magnetic field from 50 K to 300 K. But the $\rho_{xy}(\mu_0 H)$ of sample $x = 0.4$ is not linear at 300 K, which is a signature of the multiband behavior. Such multiband behaviors could be a consequence of the more complex electronic structure after the appearance of the hole pockets.

Table 2. Hall coefficients from 50 K to 300 K for $x = 0.15$, 0.25 and 0.4.

T/K	$x = 0.15$ $R_H/10^{-3}$ cm^3/C	$x = 0.25$ $R_H/10^{-3}$ cm^3/C	$x = 0.4$ $R_H/10^{-3}$ cm^3/C
50	–43.55	–34.51	–17.41
100	–31.33	–18.35	–9.35
150	–5.34	–4.06	–3.12
200	1.66	1.77	1.33
250	20.47	8.75	2.46
300	28.89	20.51	10.82

For electron-doped FeSe systems, the sign change of R_H at high temperatures is very uncommon. The Hall coefficient of both $K_xFe_{2-y}Se_2$ [18] and $(Li_{0.8}Fe_{0.2})$OHFeSe single crystals [19,20] are negative and exhibit the concave shape of R_H in the measured temperature range. Meanwhile, the R_H values of superconducting $Li_x(NH_3)_yFeSe$ crystals are also negative below room temperature but increase monotonically with temperature rising. [13] The negative R_H in heavy electron-doped FeSe is consistent with their novel electronic structure consisting of only electron pockets. We note that a sign reversal of Hall resistance with temperature increasing is only observed in another low-dimensional FeSe system — few-layered FeSe film on an $SiTO_3$ substrate, and the R_H values of 1-to-14-unit-cell (UC)-thick FeSe films show a similar crossover from electron conduction to hole conduction at $\sim$ 150 K. [22] The sign reversal of R_H observed in both FeSe films on $SrTO_3$ and the title compounds with largely expanded FeSe layers suggest the decrease of dimensionality in FeSe may play a role in the occurring of hole carriers at high temperatures.

3.6. Electronic structure

To clarify the influence of expanded FeSe layer distance on the electronic structure, the band structure of FeSe and $(C_3H_{10}N_2)_{0.32}FeSe$ (charge neutral) are calculated by first principles calculations. The orbital resolved DFT band structures from M to Γ route are presented in Fig. 7, and the more complete band structures are shown in Fig. A15. For bulk FeSe, there are four bands crossing the Fermi level, with two hole-like bands around the zone center (Γ point) and two electron-like bands around the zone corner (M point). Figures 7(c) and 7(e) show the Fermi surface for bulk FeSe, the volumes enclosed by the Fermi surface are found to be 0.230 holes/cell and 0.231 electrons/cell, respectively. The results corresponding to a carrier density of 2.93×10^{21} holes/cm^3 and 2.96×10^{21} electrons/cm^3 are in consistence with the almost compensated for electronic and hole carriers in bulk FeSe. The results are similar to the previous DFT calculations and ARPES measurements. [37,38]

By expanding the FeSe layer distance up to 10.62 Å, the band structure of $(C_3H_{10}N_2)_{0.32}FeSe$ exhibits a nearly flat dispersion along the F–Z route with a quasi-2D character, suggesting that the dispersion along the c axis is weakened as the molecule is intercalated (Fig. A15). Meanwhile, the interaction has a profound influence on the electronic structure around Γ point. As shown in Fig. 7(a), bulk FeSe has two hole pockets at Γ point, which are dominated by $d_{xz/yz}$ orbital. Notably, the molecule intercalation in $(C_3H_{10}N_2)_{0.32}FeSe$ triggers a new $d_{x^2-y^2}$ hole pocket above the Fermi level around Γ point (Fig. 7(b)). Apart from this, an empty-state band dominated by $d_{xz/yz}$ orbital sinks significantly as the FeSe layer is expanded. This sinked empty band was recently observed through STM in another low-dimensional FeSe system (1UC FeSe film on $SrTiO_3$ substrate). [39] Figures 7(d) and 7(f) show the Fermi surface for $(C_3H_{10}N_2)_{0.32}FeSe$, and the volume enclosed by the hole-like Fermi surface is found to increase significantly compared with the scenario for bulk FeSe, meanwhile, the electronic Fermi surface is almost unchanged. In particular, in the volume enclosed by Fermi surface the holes and electrons per cell are 0.791 and 0.525, namely the concentration of hole carriers and electron carriers are 5.12×10^{21} holes/cm^3 and 3.41×10^{21} electrons/cm^3, respectively. The results suggest that the quasi-2D structure will reconstruct the Fermi surface around Γ point and significantly increase the hole carrier concentration.

The heavy electron doping in FeSe is known to significantly elevate the Fermi level and sunk all the hole pockets below the Fermi energy, leaving only electron pockets in the Fermi surface (Fig. 7(g)). Meanwhile, it is also known that as

the temperature rises, the chemical potential decreases and the Fermi level sinks continually. Our first principle calculations indicate that the increase in FeSe layer distance can lift up the 'hole band' around Γ point toward Fermi energy. Therefore, the enhanced hole pockets due to low dimensionally and the reduced chemical potential at high temperature are proposed to be responsible for the sign reversal of hall resistivity in $Li_x(C_3H_0N_2)_yFe_2Se_2$ ($x = 0.15, 0.25, 0.4$).[13,40] Recently, the study of ^{77}Se, ^{7}Li, and ^{1}H nuclear magnetic resonance (NMR) of the ethylenediamine intercalated $Li_x(C_2H_8N_2)_yFe_{2-z}Se_2$ identifies strong temperature dependence of ^{77}Se NMR shift and spin-lattice relaxation rate, $1/^{77}T_1$.[41] The phenomenon is attributed to the hole-like bands moving close to the Fermi energy at high temperatures. Our observed sign reversal of R_H in $Li_x(C_3H_0N_2)_yFe_2Se_2$ proves more direct evidences that at least one of the hole pockets beneath the E_F crosses the E_F at high temperate, and thus leads to a change in the Fermi surface topology. Furthermore, considering similar band structures in intercalated FeSe and monolayer FeSe, the same picture is also applicable to the explanation of the sign reversal of Hall resistance at around 150 K in few-layered FeSe films deposited on $SiTO_3$.[42] Moreover, it is expected that the sign reversal of Hall resistance can be observed for other organic molecule intercalated FeSe materials with largely expanded layer distances.

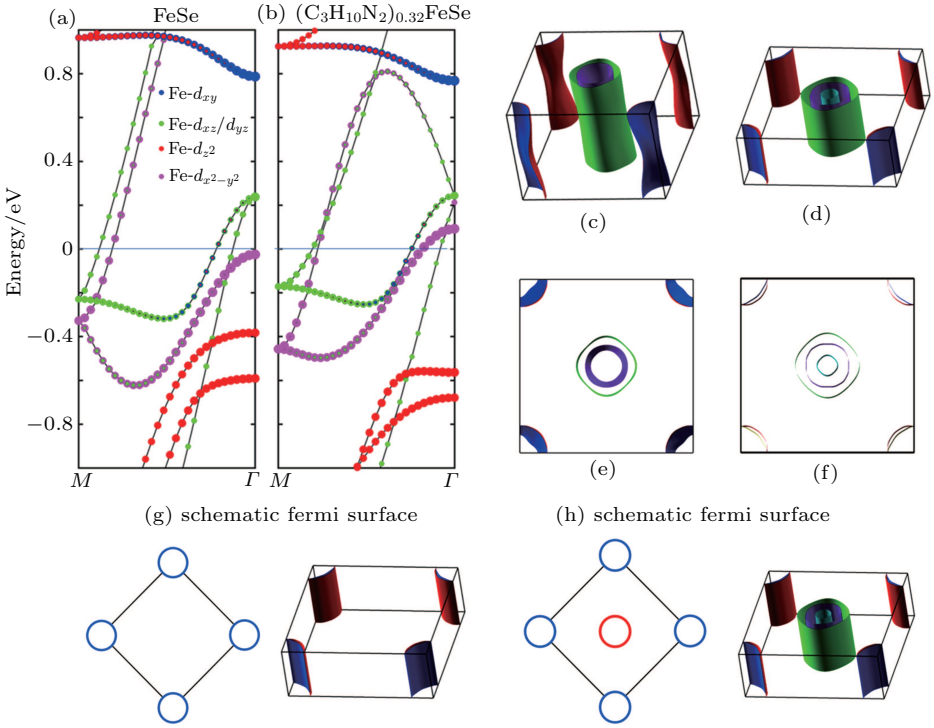


Fig. 7. Electronic structure of bulk FeSe and $(C_3H_{10}N_2)_{0.32}$FeSe. (a) and (b) Band structure along M to Γ route of bulk FeSe and $(C_3H_{10}N_2)_{0.32}$FeSe. (c) and (f) Fermi surface of bulk FeSe, $(C_3H_{10}N_2)_{0.32}$FeSe (Γ point is in the center and M point is at the corner). (g)–(h) Schematic diagram for Fermi surface of $Li_{0.15}(C_3H_{10}N_2)_{0.32}$FeSe at LT (low-temperature) and after sign change of Hall coefficient at HT (high-temperature). The Fermi energy is set to be zero.

4. Conclusions

In this work, two tetragonal superconducting phases are identified in $Li_x(C_3H_{10}N_2)_{0.32}$FeSe ($x = 0.15 \sim 0.4$) system, *i.e.*, $Li_{0.15}(C_3H_{10}N_2)_{0.32}$FeSe (phase I) and $Li_x(C_3H_{10}N_2)_{0.32}$FeSe (phase II, $0.25 < x < 0.4$). The lithium concentration is revealed as a key parameter controlling both the crystal structure and the T_c. The determined structures demonstrate that between the FeSe layers, the orientation of 1,3-DIA molecules is coupled with Li concentration, and the FeSe layer distance is expanded up to ~ 10.9 Å. Superconductivity is observed at 40 K in phase I, and the highest T_c up to 46 K is realized in phase II at $x = 0.25$. The Hall coefficient R_H values of the two phases are negative at low temperature, indicating dominant electron-type carriers due to Li doping. Meanwhile, a sign reversal of R_H at 185 K is observed in both phases and at three different doping levels, implying that the hole pockets appear in all these superconductors at high temperature. Fitting of resistivity in terms of the Lawrence–Doniach model and the measured field-dependent diamagnetic response suggests that the two superconductors belong to the quasi-2D system. Further DFT calculations reveal that the increase in FeSe layer distance will lift up a 'hole band' associated with $d_{x^2-y^2}$ character around Γ point toward Fermi energy.

Appendix A: Supplemental material

Table A1. Crystal structure parameters for phase I.

Atom	Wyckoff site	*x*	*y*	*z*	Occupation	Uiso
C1	4*h*	0.4026(8)	0.9304(4)	0.5449(7)	0.16	0.0210(7)
C2	4*h*	0.2987(4)	0.5444(3)	0.5673(9)	0.16	0.0210(7)
C3	4*h*	0.6298(5)	0.3187(2)	–0.5878(9)	0.16	0.0210(7)
N4	4*h*	0.0778(5)	1.1495(1)	0.5225(9)	0.16	0.0210(7)
N5	4*h*	0.5274(7)	–0.0595(0)	–0.6100(7)	0.16	0.0210(7)
H6	4*h*	0.5480(9)	1.0343(4)	–0.6312(1)	0.16	0.0210(7)
H7	4*h*	0.5811(3)	0.9481(9)	–0.4589(0)	0.16	0.0210(7)
H8	4*h*	0.1236(3)	0.5267(2)	–0.6543(4)	0.16	0.0210(7)
H9	4*h*	0.1495(3)	0.4414(8)	–0.4818(5)	0.16	0.0210(7)
H10	4*h*	0.8047(7)	0.3359(3)	–0.5008(8)	0.16	0.0210(7)
H11	4*h*	0.7799(5)	0.4201(8)	–0.6734(7)	0.16	0.0210(7)
H12	4*h*	0.1191(3)	1.4172(4)	–0.5612(0)	0.16	0.0210(7)
H13	4*h*	0.0257(2)	1.1667(2)	–0.4197(9)	0.16	0.0210(7)
H14	4*h*	0.2600(7)	–0.0701(4)	–0.6515(3)	0.16	0.0210(7)
H15	4*h*	0.5296(4)	–0.2033(8)	–0.5190(4)	0.16	0.0210(7)
Fe16	2*a*	0.0000	0.00000	0.0000	0.5	0.0103(4)
Fe17	2*b*	0.50000	0.50000	0.0000	0.5	0.0103(4)
Se18	2*c*	0.0000	0.50000	0.1405(3)	1.0	0.0103(4)
Li19	2*d*	0.50000	1.00000	0.2340(3)	0.065	0.0103(4)

Table A2. Crystal structure parameters for phase II.

Atom	Wyckoff site	*x*	*y*	*z*	Occupation	Uiso
C1	16*g*	0.1279(5)	0.2141(4)	0.2576(6)	0.0825	0.0210(7)
C2	16*g*	0.5162(7)	0.1725(2)	–0.2405(1)	0.0825	0.0210(7)
C3	16*g*	0.7622(7)	0.4057(2)	–0.2791(0)	0.0825	0.0210(7)
N4	16*g*	–0.0929(1)	–0.0313(0)	–0.2220(8)	0.0825	0.0210(7)
N5	16*g*	1.1401(8)	0.3796(2)	–0.2651(0)	0.0825	0.0210(7)
H6	16*g*	0.0938(2)	0.1501(1)	–0.3069(2)	0.0825	0.0210(7)
H7	16*g*	0.0523(7)	0.4949(9)	–0.2523(4)	0.0825	0.0210(7)
H8	16*g*	0.5903(5)	–0.1064(9)	–0.2459(4)	0.0825	0.0210(7)
H9	16*g*	0.5521(4)	0.2366(3)	–0.1911(5)	0.0825	0.0210(7)
H10	16*g*	0.6852(9)	0.6840(5)	–0.2739(0)	0.0825	0.0210(7)
H11	16*g*	0.7273(0)	0.3430(2)	–0.3283(9)	0.0825	0.0210(7)
H12	16*g*	–0.3510(7)	–0.0040(1)	–0.2347(4)	0.0825	0.0210(7)
H13	16*g*	–0.0819(0)	0.0322(6)	–0.1761(9)	0.0825	0.0210(7)
H14	16*g*	1.2202(6)	0.1234(8)	–0.2698(5)	0.0825	0.0210(7)
H15	16*g*	1.1824(0)	0.4421(1)	–0.2197(2)	0.0825	0.0210(7)
Fe16	4*a*	0.00000	0.00000	0.00000	1.00	0.0103(4)
Se17	4*b*	0.00000	0.50000	0.0700(3)	1.00	0.0103(4)
Li18	8*h*	0.50000	0.00000	0.12000	0.11	0.0103(4)

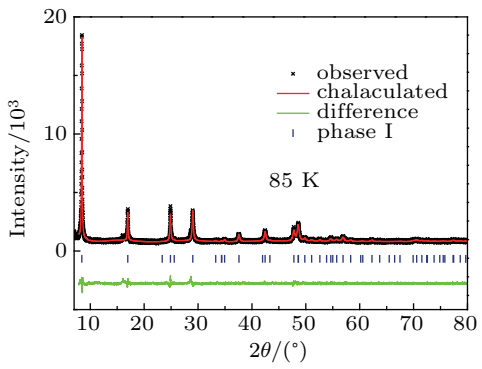


Fig. A1. Powder x-ray diffraction data for $Li_{0.13}(C_3H_{10}N_2)_{0.32}FeSe$ at 85 K.

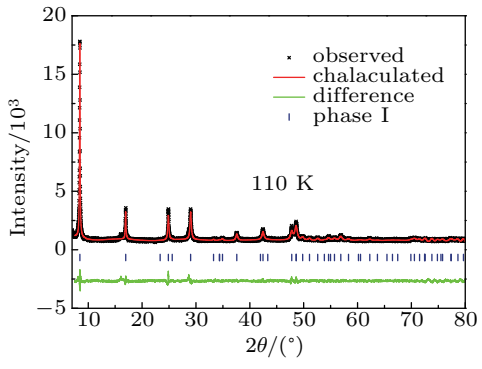


Fig. A2. Powder x-ray diffraction data for $Li_{0.13}(C_3H_{10}N_2)_{0.32}FeSe$ at 110 K.

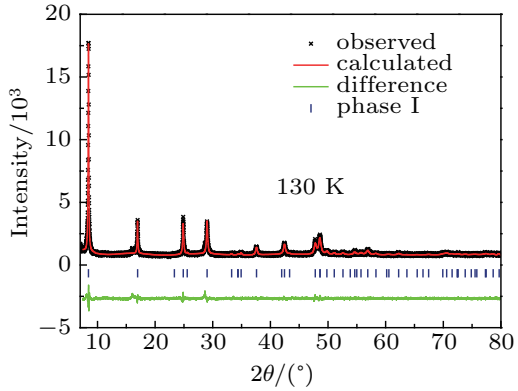


Fig. A3. Powder x-ray diffraction data for $Li_{0.13}(C_3H_{10}N_2)_{0.32}FeSe$ at 130 K.

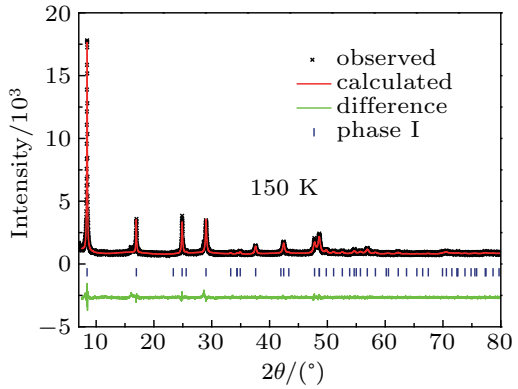


Fig. A4. Powder x-ray diffraction data for $Li_{0.13}(C_3H_{10}N_2)_{0.32}FeSe$ at 150 K.

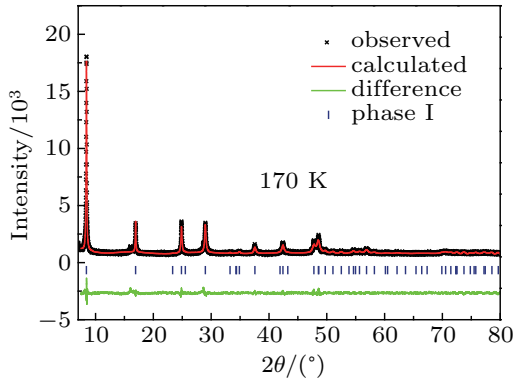


Fig. A5. Powder x-ray diffraction data for $Li_{0.13}(C_3H_{10}N_2)_{0.32}FeSe$ at 170 K.

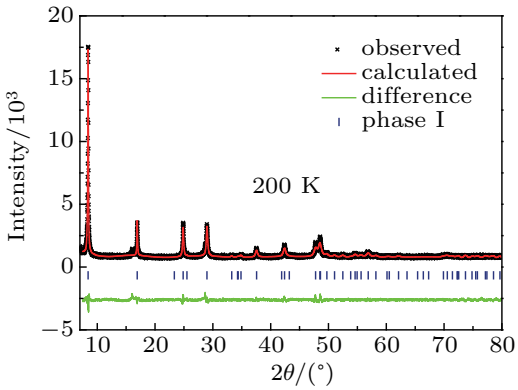


Fig. A6. Powder x-ray diffraction data for $Li_{0.13}(C_3H_{10}N_2)_{0.32}FeSe$ at 200 K.

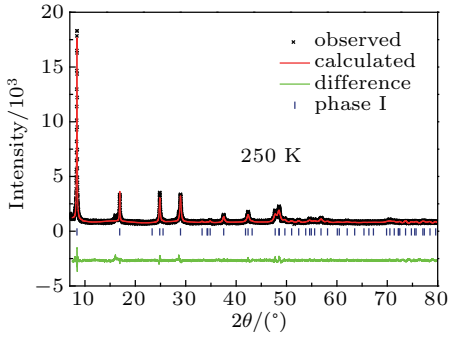


Fig. A7. Powder x-ray diffraction data for $Li_{0.13}(C_3H_{10}N_2)_{0.32}FeSe$ at 250 K.

Table A3. R_p and R_{wp} for low-temperature PXRD refinements.

Temperature/K	R_p/%	R_{wp}/%
85	3.5	4.25
110	3.87	5.78
130	3.25	4.23
150	3.95	5.01
170	4.05	5.12
200	3.26	4.12
250	3.78	4.56

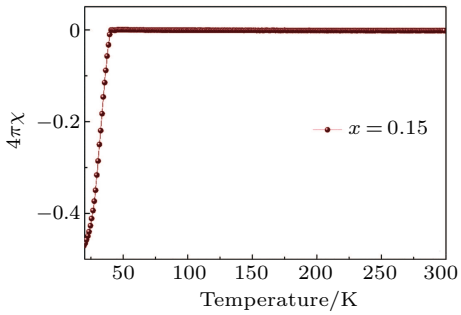


Fig. A8. Zero-field-cooled magnetic susceptibilities for $Li_{0.15}(C_3H_{10}N_2)_{0.32}FeSe$.

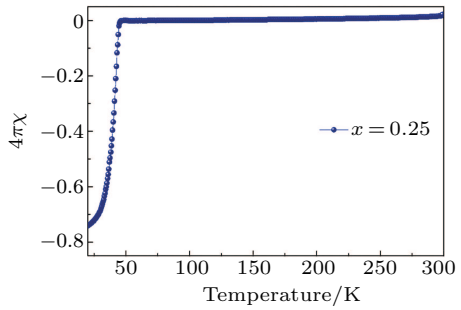


Fig. A9. Zero-field-cooled magnetic susceptibilities for $Li_{0.25}(C_3H_{10}N_2)_{0.33}FeSe$.

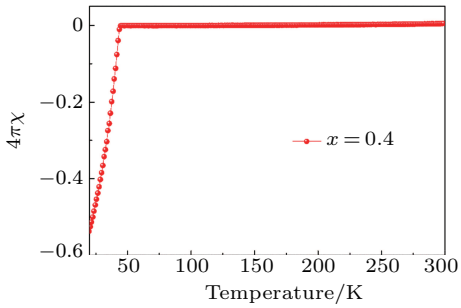


Fig. A10. Zero-field-cooled magnetic susceptibilities for $Li_{0.4}(C_3H_{10}N_2)_{0.32}FeSe$.

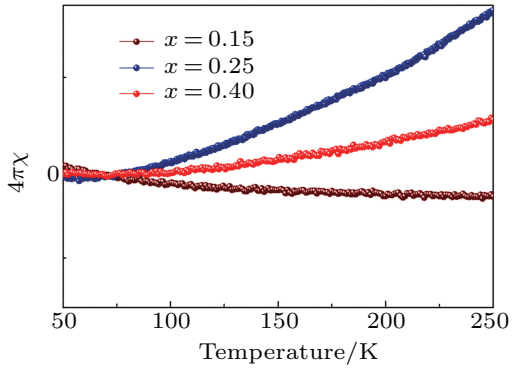


Fig. A11. Enlarged view of zero-field-cooled magnetic susceptibilities for $Li_x(C_3H_0N_2)_yFeSe$ (x = 0.15, 0.25, 0.4) from 50 K∼250 K.

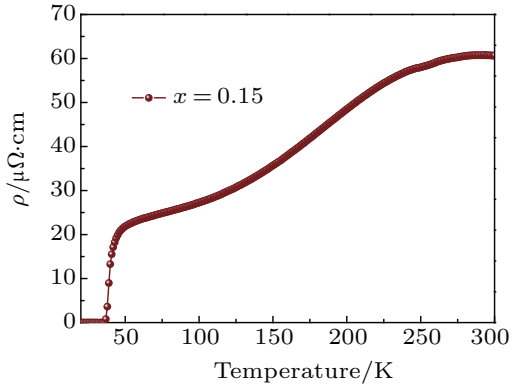


Fig. A12. Electrical resistivity of $Li_{0.15}(C_3H_{10}N_2)_{0.32}FeSe$.

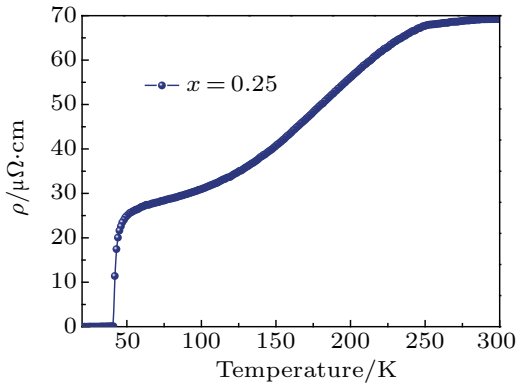


Fig. A13. Electrical resistivity of $Li_{0.25}(C_3H_{10}N_2)_{0.33}FeSe$.

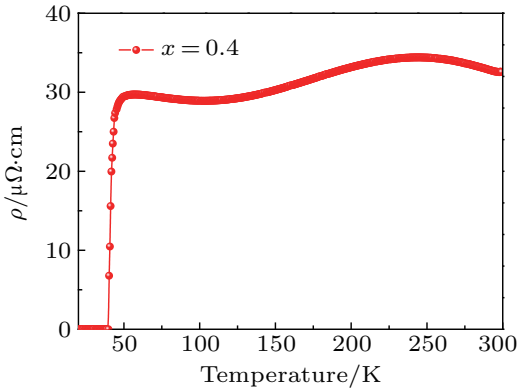


Fig. A14. Electrical resistivity of $Li_{0.4}(C_3H_{10}N_2)_{0.32}FeSe$.

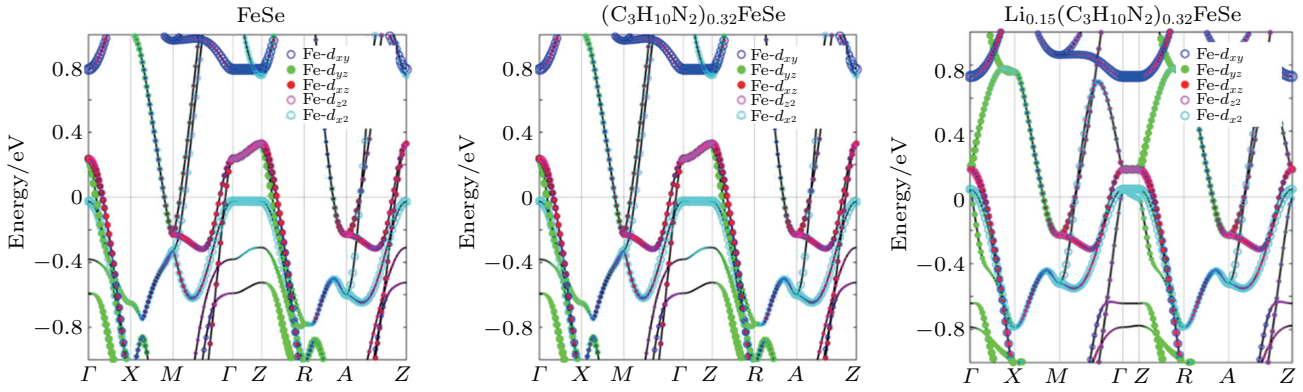


Fig. A15. Orbital resolved electronic structures of FeSe, $(C_3H_{10}N_2)_{0.32}FeSe$, and $Li_{0.15}(C_3H_{10}N_2)_{0.32}$ FeSe.

References

[1] Xu Y M, Huang Y B, Cui X, Razzoli Y E, Radovic M, Shi M, Chen G F, Zheng P, Wang N L, Zhang C L, Dai P C, Hu J P, Wang Z and Ding H 2011 *Nat. Phys.* **7** 198

[2] Mazin I I, Singh D J, Johannes M D and Du M H 2008 *Phys. Rev. Lett.* **101** 057003

[3] Wang F and Lee D H 2011 *Science* **332** 200

[4] Song C L, Wang Y L, Cheng P, Jiang Y P, Li W, Zhang T, Li Z, He K, Wang L L, Jia J F, Hung H H, Wu C J, Ma X C, Chen X and Xue Q K 2011 *Science* **332** 1410

[5] Zhang P, Yaji K, Hashimoto T, Ota Y, Kondo T, Okazaki, Wang K Z, Wen J, Gu G D, Ding H and Shin S 2018 *Science* **360** 182

[6] Guo J G, Jin S F, Wang G, Wang S C, Zhu K X, Zhou T T, He M and Chen X L 2010 *Phys. Rev. B* **82** 180520

[7] Qian T, Wang X P, Jin W C, Zhang P, Richard, Xu P G, Dai X, Fang Z, Guo J G, Chen X L and Ding H 2011 *Phys. Rev. Lett.* **106** 187001

[8] Shi X, Han Z Q, Peng X L, Richard P, Qian T, Wu X X, Qiu M W, Wang S C, Hu J P, Sun Y J and Ding H 2017 *Nat. Commun.* **8** 14988

[9] Lu X F, Wang N Z, Wu H, Wu Y P, Zhao D, Zeng X Z, Luo X G, Wu T, Bao W, Zhang G H, Huang F Q, Huang Q Z and Chen X H 2015 *Nat. Mater.* **14** 325

[10] Ren M, Yan Y, Niu X, Tao R, Hu D, Peng R, Xie B, Zhao J, Zhang T and Feng D L 2017 *Sci. Adv.* **3** e1603228

[11] Zhao L, Liang A, Yuan D, Hu Y, Liu D, Huang J, He S, Shen B, Xu Y, Liu X, Yu L, Liu G, Zhou H, Huang Y, Zhou X, Liu F K, Lu Z, Zhao Z, Chen C, Xu Z and Zhou X J 2016 *Nat. Commun.* **7** 10608

[12] McQueen T M, Williams A J, Stephens P W, Tao J, Zhu Y, Ksenofontov V, Casper F, Felser C and Cava R J 2009 *Phys. Rev. Lett.* **103** 057002

[13] Sun S, Wang S, Yu R and Lei H 2017 *Phys. Rev. B* **96** 064512

[14] Lei H, Graf D, Hu R, Ryu H, Choi E S, Tozer S W and Petrovic C 2012 *Phys. Rev. B* **85** 094515

[15] Margadonna S, Takabayashi Y, Ohishi Y, Mizuguchi Y, Takano Y, Kagayama T, Nakagawa T, Takata M and Prassides K 2009 *Phys. Rev. B* **80** 064506

[16] Medvedev S, McQueen T M, Troyan I A, Palasyuk T, Eremets M I, Cava R J, Naghavi, Casper S F, Ksenofontov V, Wortmann G and Felser C 2009 *Nat. Mater.* **8** 630

[17] Sun J P, Ye G Z, Shahi P, Yan J Q, Matsuura K, Kontani H, Zhang G M, Zhou Q, Sales B C, Shibauchi T, Uwatoko Y, Singh D J and Cheng J G 2017 *Phys. Rev. Lett.* **118** 147004

[18] Ding X, Pan Y, Yang H and Wen H H 2014 *Phys. Rev. B* **89** 224515

[19] Lei B, Xiang Z J, Lu X F, Wang N Z, Chang J R, Shang C, Zhang A M, Zhang Q M, Luo X G, Wu T, Sun Z and Chen X H 2016 *Phys. Rev. B* **93** 060501

[20] Dong X, Jin K, Yuan D, Zhou H, Yuan J, Huang Y, Hua W, Sun J, Zheng P, Hu W, Mao Y, Ma M, Zhang G, Zhou F and Zhao Z 2015 *Phys. Rev. B* **92** 064515

[21] Sun J P, Shahi P, Zhou H X, Huang Y L, Chen K Y, Wang B S, Ni S L, Li N N, Zhang K, Yang W G, Uwatoko, Xing Y G, Sun J, Singh D J, Jin K, Zhou F, Zhang G M, Dong X L, Zhao Z X and Cheng J G 2018 *Nat. Commun.* **9** 380

[22] Zhao W, Li M, Chang C Z, Jiang J, Wu L J, Liu C X, Jagadeesh S, Moodera, Zhu Y M and Chan H W 2018 *Sci. Adv.* **4** eaao2682

[23] Dewald R R and Dye J L 1964 *J. Phys. Chem.* **68** 122

[24] Kresse G and Furthmüller J 1996 *Phys. Rev. B* **54** 11169

[25] Kresse G and Furthmüller J 1996 *Comp. Mater. Sci.* **6** 15

[26] Perdew J P, Burke K and Ernzerhof M 1996 *Phys. Rev. Lett.* **77** 3865

[27] Burrard-Lucas M, Free D G, Sedlmaier S J, Wright J D, Cassidy S J, Hara Y, Corkett A J, Lancaster T, Baker P J, Blundell S J and Clarke S J 2013 *Nat. Mater.* **12** 15

[28] Ying T P, Chen X L, Wang G, Jin S F, Lai X F, Zhou T T, Zhang H, Shen S J and Wang W Y 2013 *J. Am. Chem. Soc.* **135** 2951

[29] Young V G, McKelvy M J, Glaunsinger W S and Dreele von R B 1988 *Solid State Ion.* **26** 47

[30] Sóñora D, Carballeira C, Ponte J J, Xie T, Luo H Q, Li S L and Mosqueira J 2017 *Phys. Rev. B* **96** 014516

[31] Rey R I, Carballeira C, Mosqueira J, Salem-Sugui S, Alvarenga A D, Luo H Q, Lu X Y, Chen Y C and Vidal F 2013 *Supercond Sci. Technol.* **26** 055004

[32] Hikami S and Larkin A I 1988 *Mod. Phys. Lett. B* **2** 693

[33] Kes P H, Beek van der C J, Maley M P, McHenry M E, Huse D A, Menken M J V and Menovsky A A 1991 *Phys. Rev. Lett.* **67** 2383

[34] Lang M, Steglich F, Toyota N and Sasaki T 1994 *Phys. Rev. B* **49** 15227

[35] Welp U, Fleshler S, Kwok W K, Klemm R A, Vinokur V M, Downey J, Veal B and Crabtree G W 1991 *Phys. Rev. Lett.* **67** 3180

[36] Du Z Y, Yang X, Altenfeld D, Gu Q Q, Yang H, Eremin I, Hirschfeld P J, Mazin I I, Lin H, Zhu X Y and Wen H H 2018 *Nat. Phys.* **14** 134

[37] Subedi Alaska, Zhang L J, Singh D J and Du M H 2008 *Phys. Rev. B* **78** 134514

[38] Nakayama K, Miyata Y, Phan G N, Sato T, Tanabe Y, Urata T, Tanigaki K and Takahashi T 2014 *Phys. Rev. Lett.* **113** 237001

[39] Huang D, Song C L, Webb T A, Fang S, Chang C Z, Moodera J S, Kaxiras E and Hoffman J E 2015 *Phys. Rev. Lett.* **115** 017002

[40] Li C H, Sun S S, Wang S H and Lei H C 2017 *Phys. Rev. B* **96** 134503

[41] Hrovat M M, Jeglic P, Klanjsek M, Hatakeda T, Noji T, Tanabe Y, Urata T, Huynh K K, Koike Y, Tanigaki K and Arcon D 2015 *Phys. Rev. B* **92** 094513

[42] Rebec S N, Jia T, Zhang C, Hashimoto M, Lu D H, Moore R G and Shen Z X 2017 *Phys. Rev. Lett.* **118** 067002